







Open Archive Toulouse Archive Ouverte (OATAO)

OATAO is an open access repository that collects the work of Toulouse researchers and makes it freely available over the web where possible

This is an author's version published in: <http://oatao.univ-toulouse.fr/19785>

Official URL: <https://doi.org/10.1007/s10854-016-5471-8>

To cite this version:

Ben Jemaa, Imen and Chaabouni, Fatma and Presmanes, Lionel  and Thimont, Yohann  and Abaab, Mohamed and Barnabé, Antoine  and Tailhades, Philippe  *Structural, optical and electrical investigations on Nb doped TiO₂ radio-frequency sputtered thin films from a powder target.* (2016) *Journal of Materials Science: Materials in Electronics*, 27 (12). 13242-13248. ISSN 0957-4522

Any correspondence concerning this service should be sent to the repository administrator: tech-oatao@listes-diff.inp-toulouse.fr

Structural, optical and electrical investigations on Nb doped TiO₂ radio-frequency sputtered thin films from a powder target

I. Ben Jemaa^{1,2} · F. Chaabouni¹ · L. Presmanes³ · Y. Thimont³ · M. Abaab¹ · A. Barnabe³ · P. Tailhades³

Abstract Pure and Nb doped TiO₂ (TNO) thin films were deposited onto glass substrates by RF magnetron sputtering technique using a Nb and TiO₂ mixture powder target at room temperature to explore the possibility of producing sputtered TNO films by a low cost process. The effect of Nb doping on the structure, morphology, optical and electrical properties of the prepared films was studied by systematically varying the Nb content from 2 to 6 wt%. GXRD results show that the deposited films mainly possess rutile phase with the (110) orientation. Raman spectra confirm that the deposited films are predominantly rutile phase. Surface roughness increases with the increase of Nb doping concentration, which may be attributed to the structural changes in the film due to the incorporation of Nb into the TiO₂ lattice. Optical transmittance in the visible range reaches 85 % for the undoped films then it decreases as the doping content increases. Doping by niobium resulted in a slight increase in the optical band gap energy of the films due to the Burstein–Moss effect. The resistivity measurement of TNO films reveals that the Nb doping improves the electrical conductivity of the deposited films compared to the undoped one. The best value was observed for films deposited at 4 wt% Nb.

1 Introduction

Titanium dioxide is a material that has always been the subject of much researches and has attracted much interest because of its unique combination of chemical and physical outstanding properties which make it a promising candidate for future technology of thin films and optoelectronic applications. The crystal form of TiO₂ is commonly composed of three crystalline polymorphs: anatase, brookite and rutile. Among them, rutile exhibits many interesting optical characteristics and it is thermodynamically the most stable phase [1]. Moreover, rutile TiO₂ film has high refractive index, excellent optical transmittance and high chemical stability allowing its use in optical coating such as dielectric interference filters and antireflective coating. Rutile TiO₂ has also attracted a great deal of interest for use in fabricating capacitors in microelectronics devices owing to its high dielectric constant and high resistivity [2]. Great efforts have been devoted to improve properties of TiO₂ through doping with transition metal ions (such as Nb, Fe, Mo, etc.), which contributes to the increase in application areas [3–5]. Nb doped TiO₂ could also be an interesting substitute material for the high-cost indium-tin-oxide as transparent electrodes [6]. Several techniques can be used to obtain Nb-doped TiO₂ thin films, such as sol–gel method [7], pulsed laser deposition (PLD) [8, 9], reactive DC sputtering [10], and radio-frequency (RF) magnetron sputtering [4], etc. Among them, the sputtering technique can perform high deposition rates at room temperature, with no toxic gas emissions; Furthermore, it is an attractive method for the preparation of thin films with high quality and high uniformity on large scale which makes it suitable for industrial application [11]. The ceramic targets are very sensitive to the high resistance, which causes many problems with cracking during deposition [12]. So, it is

✉ I. Ben Jemaa
i_benjemmaa@yahoo.fr

¹ Ecole Nationale d'Ingénieurs de Tunis, Laboratoire de Photovoltaïque et Matériaux Semi-conducteurs, Université de Tunis El Manar, 1002 Tunis, Tunisia

² Département de Physique, Faculté des Sciences de Bizerte, Université de Carthage, 7021 Zarzouna, Bizerte, Tunisia

³ CIRIMAT, Université de Toulouse, CNRS, INPT, UPS, Université de Toulouse 3 Paul Sabatier, 118 route de Narbonne, 31062 Toulouse Cedex 9, France

important to explore a new method to fabricate the sputtering targets by a low cost process.

In this work, TiO₂ thin films with rutile phase have been deposited on glass substrates by RF magnetron sputtering using a powder target at room temperature. The structural, morphological, optical and electrical properties influenced by Nb incorporated at different content have been systematically investigated.

2 Experimental details

2.1 Deposition process

Undoped and Nb-doped TiO₂ (TNO) thin films were deposited onto glass substrates at room temperature by RF magnetron sputtering technique using a powder target. Nb (neyco, 99.9 %) powder was added to a TiO₂ (neyco, 99.99 %) powder as a dopant then blended in a crusher for several minutes to get uniform compositions. The mixture was distributed across the surface of a copper backing plate on the magnetron, lightly tamped down to produce a 2 mm uniform thickness. No further processes were involved in target production. The Nb doping content was adjusted at 2, 4 and 6 wt% (the relative mole ratios of the Nb to the TiO₂ were given in Table 1). Before deposition, the vacuum chamber was evacuated to a base pressure below 10⁻⁴ Pa by the combined action of rotary and diffusion pumps. Sputtering was performed in pure Ar (sputter gas) at a constant power density of 3.1 W/cm². Glass substrates were previously cleaned with washing agents (detergent, ethanol and de-ionized water) followed by degreasing with acetone in an ultrasonic bath, before being introduced into the vacuum system. Argon gas was introduced into the chamber through a mass flow controller operated at 5 sccm to get a deposition pressure of 0.3 Pa. The typical deposition time was 5 h. The substrates were rotated (15 rd/min) and placed parallel to the target surface at a distance of 65 mm. The target surface was pre-sputtered for 15 min in order to remove surface contamination.

2.2 Characterization techniques

Structural characterizations of the films were performed by grazing angle X-ray diffraction (GXRD) (grazing angle $\alpha = 1^\circ$) on a Siemens D 5000 diffractometer using the copper K α radiation and equipped with a Bruker Sol-X

Table 1 Relative mole ratios of the Nb to the TiO₂

wt% of Nb in the target	0	2	4	6
Nb/TiO ₂ molar ratio	0	0.017	0.035	0.054

detector. Raman scatterings were measured using a Jobin Yvon T64000 spectrometer with a laser excitation wavelength of 488 nm. To study the microstructure of the films, Atomic Force Microscopy (AFM) Nanoscope III Dimension 3000 was used. Optical measurements of the total transmittance (T_T) and the total reflectance (R_T) spectra at near normal incidence were performed in the wavelength range from 300 to 1100 nm using a UV/Visible/IR integrated spectrophotometer (Bentham PVE 300), and then the spectra were modeled using the SCOUT software [13]. Film thickness was deduced both from optical simulations and from Swanepoel procedure [14] which is based on the use of the extremes of the interference fringes.

Films resistivity was determined at room temperature by a four point measuring device composed of a source measure unit KEITHLEY 237, a high temperature four point probe QUAD PRO Resistivity System and a temperature controller SIGNATONE model S-1060R.

3 Results and discussion

3.1 Structural properties

The GXRD patterns of the TiO₂ and TNO films deposited on glass substrates with different Nb content are shown in Fig. 1. It is quite clear from this figure that irrespective of the doping level of Nb, all the films are polycrystalline and belong to the rutile structure with its (110), (101), (200), (211) and (220) characteristic Bragg's reflexions. It is also clear from Fig. 1 at $2\theta \approx 27.4^\circ$ that the films exhibit a (110) preferred orientation. Diffraction peaks corresponding to niobium metal or oxides such as NbO, Nb₂O₅ or any mixed oxides were not observed in the XRD patterns, while

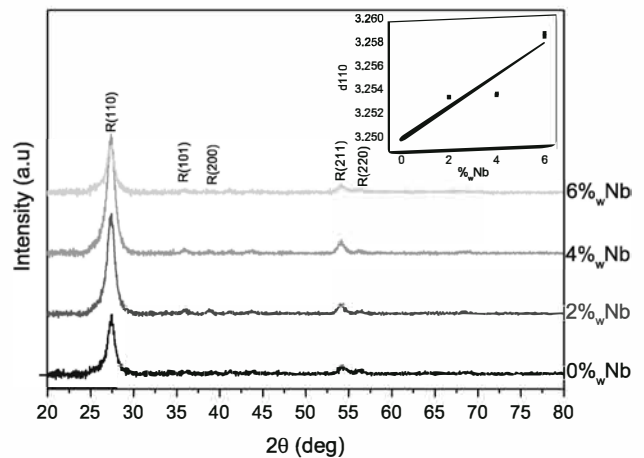


Fig. 1 X-ray diffraction patterns of the TiO₂ and TNO films deposited at different Nb content. Inset variation of the d(110) values versus. Nb content

the (110) peak position is linearly shifted to the lower 2θ values with the increase of Nb content. This can be attributed to the fact that the Nb ions were inserted into the TiO_2 lattice sites. The $d(110)$ values are plotted as a function of the Nb content in the inset of Fig. 1. An increase of the lattice spacing $d(110)$ was observed with the increase of the Nb content verifying the Vegard's law [15] and indicating the substitution of Ti^{4+} by Nb^{5+} in the TiO_2 lattice due to the relative sizes of the cations ($r(\text{Nb}^{5+}) = 0.64 \text{ \AA}$ and $r(\text{Ti}^{4+}) = 0.605 \text{ \AA}$ according to Shannon [16]). The intensity of the diffraction peaks was found to increase with the increase of the Nb doping content up to 4 wt%. It is partially due to thickness increase (the thickness was calculated by Swanepoel method as will be discussed in optical section, see Table 2) but it can also be on account of crystallinity improvement. However, at higher doping content 6 wt%, even if the film is slightly thicker, the reflected intensity at (110) plane appears to decrease. The drop in the peak intensity may be due to the high doping content which can lead to the formation of stress, to the excessive replacement of Ti^{4+} ions with Nb^{5+} ions in the lattice of the TiO_2 films that decrease the crystallinity, or to the co-precipitation of nanocrystalline or quasi-amorphous Nb oxides at the grain boundaries not observable by diffraction study.

The crystallite size can be estimated from the reflected intensity at (110) plane by the GXR D data using the Debye-Scherrer formula [17]:

$$D = \frac{0.9\lambda}{\beta \cos \theta} \quad (1)$$

where D is the average crystallite size, λ is the X-ray wavelength, θ is the diffraction angle of the peak and β is the sample size contribution to the overall Full Width at Half Maximum. The average crystallite size was found to be of about 20 nm for the studied films showing that the films were nanostructured.

3.2 Raman measurements

To confirm the purity of our films, we report the characterization by Raman spectroscopy. The rutile and anatase phases have very distinct Raman active modes. Rutile TiO_2 has four Raman active modes, A_{1g} (612 cm^{-1}), B_{1g} (143 cm^{-1}), B_{2g} (826 cm^{-1}) and E_g (447 cm^{-1}), and

anatase TiO_2 has six Raman active modes, A_{1g} (515 cm^{-1}), 2 B_{1g} ($399, 519 \text{ cm}^{-1}$) and 3 E_g ($144, 197, 639 \text{ cm}^{-1}$) [18–21]. Figure 2 shows Raman spectra of the TiO_2 and TNO films prepared by RF magnetron sputtering at various Nb content. Two main peaks were observed at 449 and 613 cm^{-1} which can be attributed to the rutile phase (E_g and A_{1g}). Raman results provide evidence that all the films are of rutile phase. This observation is consistent with the GXR D results. A slight shift in the position of E_g Raman bands is observed when both the amount of Nb and the film thickness increase, which can be due to the presence of stress in the samples [22].

3.3 Surface morphology

The morphological characteristic of TiO_2 and TNO thin films has been studied using atomic force microscopy (AFM). The surface topographical images recorded for the TiO_2 and TNO films at various Nb content are shown in Fig. 3. These images reveal that all the samples present a granular morphology. It can be seen that the increase in Nb doping affects the surface morphology of the samples. Surface roughness increases with the increase of the Nb doping content, which may be attributed to the structural changes in the film due to the incorporation of Nb into the TiO_2 lattice. The root mean square (RMS) roughness

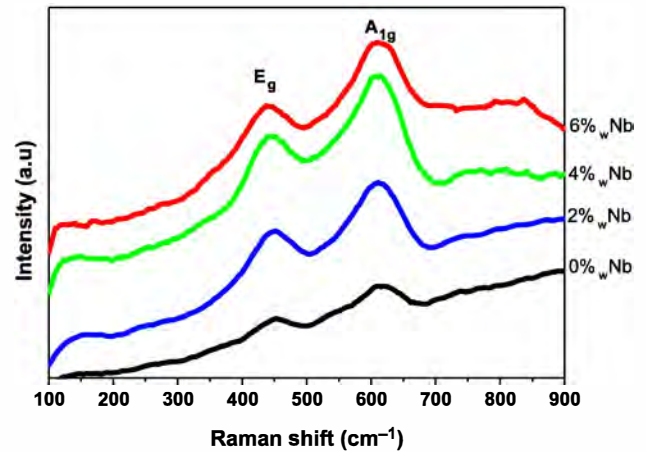


Fig. 2 Raman spectra of the TiO_2 and TNO thin films at various Nb content

Table 2 Estimated thicknesses (d) and optical parameters of the TiO_2 and TNO films

Sample	d (nm) swanepoel	d (nm) simulation	E_g (eV)	n (at $\lambda = 600 \text{ nm}$)	E_U (meV)
Nb 0 wt%	260	275	3.44	2.40	250
Nb 2 wt%	277	297	3.45	2.43	260
Nb 4 wt%	312	325	3.49	2.54	270
Nb 6 wt%	363	362	3.47	2.58	330

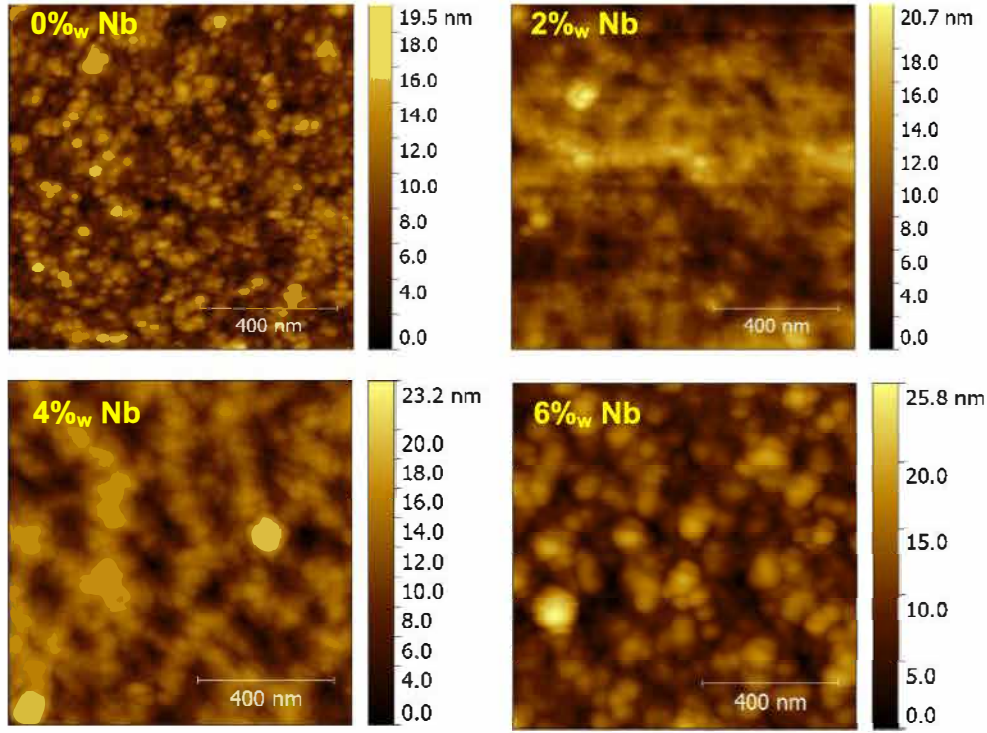


Fig. 3 AFM surface morphology images of the TiO₂ and TNO thin films at various Nb content

values were found to be equal to 2.18, 2.37, 2.61 and 2.87 nm for undoped and Nb-doped TiO₂ thin films at 2, 4 and 6 wt%, respectively. We note also that the average grain size increases from 25 to 45 nm with the increase of the Nb content from 0 to 6 wt%, respectively.

3.4 Optical study

Figure 4a shows the total optical transmittance spectra in the wavelength range of 300–1100 nm for TiO₂ and TNO films at different Nb content. It is clear from Fig. 4a that the total transmittance spectra for all the films exhibit interference fringes confirming the optical homogeneity and the uniformity of the surface. The deposited films are transparent in the visible region, with a transmittance ranging from 60 to 85 %, depending on the dopant content. The UV region is characterized by a strong absorption edge due to the inter-band electronic transition. Figure 4a also shows that the average transmittance decreases with the increase in the Nb doping content. This decrease may be due to the increased scattering of photons by crystal defects created by doping.

3.4.1 Optical band gap

The optical band gap (E_g) is correlated to the optical absorption coefficient (α) by the following formula [23]:

$$\alpha h\nu = A(h\nu - E_g)^n \quad (2)$$

where, $h\nu$ is the photon energy, A is a constant characteristic of the semiconductor which does not depend on $h\nu$, E_g is the optical band gap and n is related to the nature of the fundamental optical transition. n is theoretically equal to 1/2, 2, 3/2 or 3 for direct allowed, indirect allowed, direct forbidden and indirect forbidden transitions, respectively. In the present study, the value of ' n ' is taken as 1/2 due to the direct band gap of the TiO₂ rutile phase. In order to calculate the optical band gap energy (E_g) of the thin films, the fundamental absorption α can be estimated using the relation [24]:

$$\alpha = \frac{1}{d} \ln \left[\frac{(1 - R_T)^2}{T_T} \right] \text{ cm}^{-1} \quad (3)$$

where T_T is the total transmittance, R_T is the total reflectance and d is the film thickness. The film thickness d was estimated from Swanepoel procedure [14] and determined by optical simulation. The values of d are given in Table 2. Figure 4b shows $(\alpha h\nu)^2$ plotted as a functions of photon energy for the TiO₂ and TNO thin films grown at various contents of Nb. The optical band gap can be obtained by extrapolating the corresponding straight line portion. The obtained values of the optical energy gap of the undoped and TNO films are listed in Table 2. The optical band gap

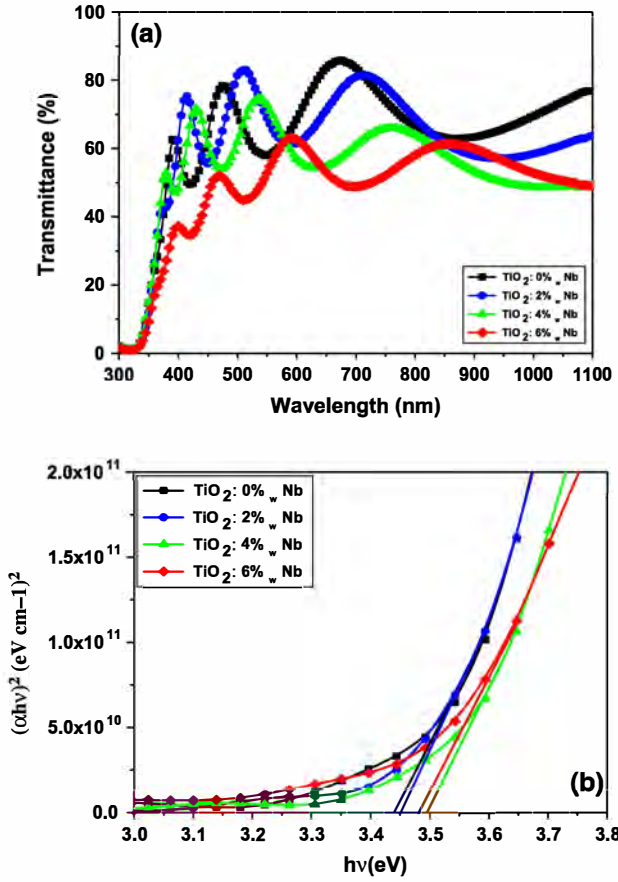


Fig. 4 a Optical transmittance spectra of the TiO₂ and TNO thin films deposited at different Nb Content. b $(\alpha h\nu)^2$ versus $h\nu$ plots for the TiO₂ and TNO thin films at different Nb content

shifted towards higher energies with the incorporation of the Nb. Similar results are also observed in the bibliography for sputter-deposited TiO₂:Nb films [25–27]. The widening of E_g can be primarily explained by the well-known Burstein–Möss (BM) effect [28], in which the lowest states in the conduction band are blocked, and transitions can take place only at higher energies level in conducting band. This effect is often observed in degenerated semiconductors. Therefore, it is believed that the blue shift of the optical band gap imply an increase in the carrier density with the increase in the Nb content [25].

3.4.2 Urbach energy

The incorporation of impurity into the semiconductor often reveals the formation of band tailing in the band gap. In order to evaluate the disorder caused by defects and doping in thin films, we estimated the Urbach energy tailing of the optical absorption edge in the layers follows the empirical Urbach law [29]:

$$\alpha = \alpha_0 \exp\left(\frac{h\nu}{E_U}\right) \quad (4)$$

where α_0 is a constant, the following relation was used to calculate the E_U values for the TiO₂ and TNO thin films:

$$E_U = [d(\ln \alpha)/d(h\nu)]^{-1} \quad (5)$$

The experimental value of the Urbach energy was estimated from the slope of $(\ln \alpha)$ versus energy $h\nu$ plots of the films. The E_U values are summarized in Table 2. It is remarkable that Urbach energy increases with the Nb content in TiO₂. In addition, doping may promote defect states that can trap charge carriers. These localized charge carriers can jump between these defect states [30, 31].

3.4.3 Refractive index

The Swanepoel’s method [14] was used to calculate the refractive index n . This method suggests creating an upper and lower envelope of the transmittance spectrum beyond the absorption edge. The refractive index can then be calculated from the relation [14]:

$$n = \sqrt{N + \sqrt{N^2 - n_S^2}} \quad (6)$$

where

$$N = 2n_S \frac{T_{T_{\max}} - T_{T_{\min}}}{T_{T_{\max}} T_{T_{\min}}} + \frac{n_S^2 + 1}{2} \quad (7)$$

Here n_S is the refractive index of the glass substrate. $T_{T_{\max}}$ and $T_{T_{\min}}$ are the values of the envelope at maximum and minimum positions defined at the same wavelength of the total transmittance spectra, respectively. From Fig. 5, an increase in the refractive index is observed with the increase in the Nb content (see Table 2), which means that

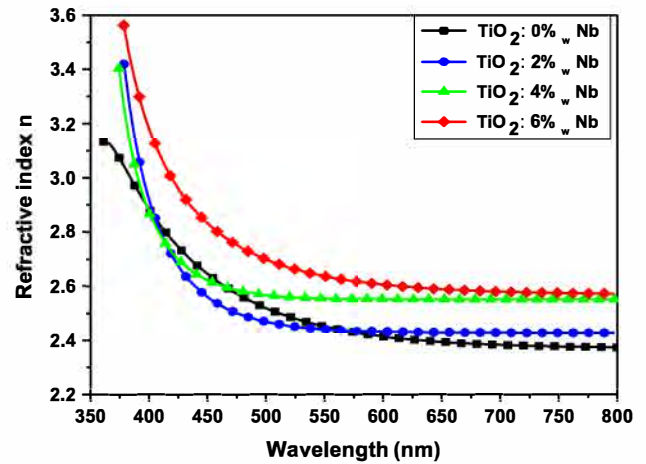


Fig. 5 Refractive index n plotted as a function of wavelength for the TiO₂ and TNO thin films at various Nb content

the films turn out to be more opaque as the Nb doping increases.

4 Electrical properties

The resistivity values as a function of Nb content are shown in Fig. 6. As we can see, the undoped TiO_2 films are resistive with a resistivity value of $7.1 \times 10^1 \Omega \text{ cm}$. It is also clear that by increasing the Nb doping content, the resistivity decreases sharply to a value of $3.4 \times 10^0 \Omega \text{ cm}$ for 2 wt% Nb and a value of $6.40 \times 10^{-1} \Omega \text{ cm}$ for 4 wt% Nb, which means an improvement of the electrical conductivity by two orders of magnitude. The best value is obtained for films doped with 4 wt% Nb. With more increasing Nb doping content typically at 6 wt%, the resistivity increases (to $2.55 \times 10^0 \Omega \text{ cm}$) compared to that of 4 wt% Nb. The increase in the films resistivity may be related to the presence of atomic disorders and high scattering in the lattice structure. Also, based on the GXR D patterns, the increase in the resistivity may be due to the increase in disorders because the intensity of the (110) diffraction peak for the 6 wt% Nb doping decreases.

5 Figure of merit

The figure of merit (FOM) defined by Haacke provides a useful tool to comparing the performance of TCO films. It is defined as [32]:

$$FOM = \frac{T^{10}}{R_s} \quad (8)$$

where T is the average visible transmittance and R_s is the sheet resistance.

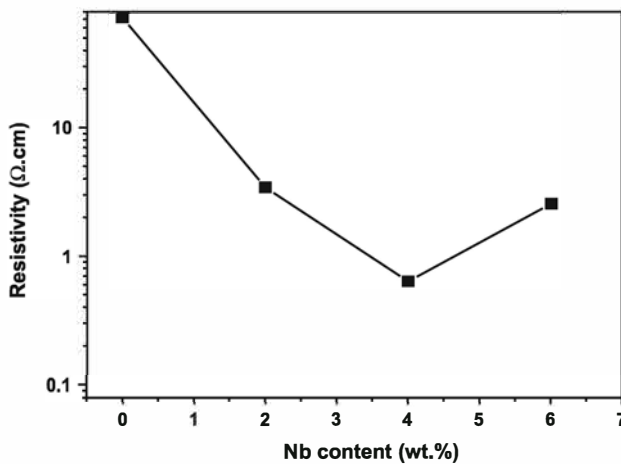


Fig. 6 Resistivity as a function of Nb content for the TiO_2 and TNO films

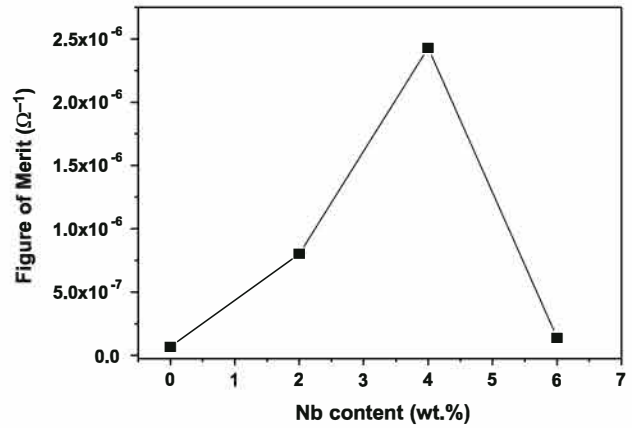


Fig. 7 Figure of merit of the TNO thin films at different Nb content

The Fig. 7 shows the FOM of the TNO thin films prepared as a function of Nb content. The FOM value increased with the increase in the Nb content up to 4 wt% reaching the highest value of $2.43 \times 10^{-6} \Omega^{-1}$ then decreased with further Nb doping content. The decrease of FOM above 4 wt% is due to the increase of electrical resistivity and the lower transmittance compared to the other films. These results prove that the 4 wt% Nb content is the optimal doping concentration of the deposited TNO thin films.

6 Conclusion

Both pure and TNO films deposited at different Nb content by RF magnetron sputtering technique using a powder target at room temperature have been investigated. GXR D patterns revealed that the deposited films exhibit a rutile phase with the preferred (110) orientation. Raman spectra confirmed the presence of the rutile phase in all the samples. No characteristic peaks of niobium oxide were observed in the Nb doped TiO_2 thin films which may result from the incorporation of Nb in the TiO_2 lattice. The films are transparent in the visible region. Moreover, transmittance was found to decrease with the increase in the Nb doping content. Doping by niobium resulted in a slight increase in the optical band gap energy of the films due to the Burstein–Moss effect. The decrease in the resistivity of the Nb doped films compared to that of undoped one was observed, showing an improvement of the conductivity with Nb doping and confirming the donor action of Nb on Ti lattice sites. The best values of conductivity and FOM were observed for films deposited with 4 wt% Nb. RF sputtering from a powder target was found to be a simple technique for the synthesis of nano-structures TNO thin films with rutile phase at room temperature without extra energy input. In order to meet the required specifications of

TCOs for application in electrodes, the electrical properties of TNO still need further improvement.

References

1. S.S. Pradhan, S.K. Pradhan, V. Bhavanasi, *Thin Solid Films* **520**, 1809 (2012)
2. S.-F. Wang, Y.-F. Hsu, R.-L. Lee, Y.-S. Lee, *Appl. Surf. Sci.* **229**, 140–147 (2004)
3. R. Subasri, M. Tripathi, K. Murugan, J. Revathi, G.V.N. Rao, T.N. Rao, *Mater. Chem. Phys.* **124**, 63–68 (2010)
4. T. Potlog, P. Dumitriu, M. Dobromir, A. Manole, D. Luca, *Mater. Des.* **85**, 558–563 (2015)
5. A. Kubacka, G. Colón, M. Fernández-García, *Catal. Today* **143**, 286–292 (2009)
6. A.V. Manole, M. Dobromir, M. Gîrtan, R. Mallet, G. Rusu, D. Luca, *Ceram. Int.* **39**, 4771–4776 (2013)
7. M.Z. Atashbar, H.T. Sun, B. Gong, W. Wlodarski, R. Lamb, *Thin Solid Films* **326**, 238–244 (1998)
8. T. Hitosugi, A. Ueda, S. Nakao, N. Yamada, Y. Furubayashi, Y. Hirose, T. Shimada, T. Hasegawa, *Appl. Phys. Lett.* **90**, 212106 (2007)
9. Y. Furubayashi, T. Hitosugi, Y. Yamamoto, K. Inaba, G. Kinoda, Y. Hirose, T. Shimada, T. Hasegawa, *Appl. Phys. Lett.* **86**, 252101 (2005)
10. N. Oka, Y. Sanno, J. Jia, S.-I. Nakamura, Y. Shigesato, *Appl. Surf. Sci.* **301**, 551–556 (2014)
11. P.B. Nair, V.B. Justinictor, G.P. Daniel, K. Joy, V. Ramakrishnan, P.V. Thomas, *Appl. Surf. Sci.* **257**, 10869–10875 (2011)
12. Y. Bouzmit, Y. Beggah, K. Djessas, *J. Sol-Gel Sci. Technol.* **61**, 449 (2012)
13. W. Theiss; Hard & Software. <http://www.mtheiss.com>
14. R. Swanepoel, *J. Phys. E Sci. Instrum.* **16**, 1214 (1983)
15. A.R. Denton, N.W. Ashcroft, *Phys. Rev. A* **43**, 3161 (1991)
16. R.D. Shannon, *Acta Cryst. A* **32**, 751–767 (1976)
17. W. Zhang, S. Zhu, Y. Li, F. Wang, *J. Mater. Sci. Technol.* **20**, 31–34 (2004)
18. A. Li Bassi, D. Cattaneo, V. Russo, C.E. Bottani, E. Barborini, T. Mazza, P. Piseri, P. Milani, F.O. Ernst, K. Wegner, S.E. Pratsinis, *J. Appl. Phys.* **98**, 074305 (2005)
19. H. Wang, Y. Li, X. Ba, L. Huang, Y. Yu, *Appl. Surf. Sci.* **345**, 49–56 (2015)
20. C. Tealdi, E. Quartarone, P. Galinetto, M.S. Grandi, P. Mustarelli, *J. Solid State Chem.* **199**, 1–6 (2013)
21. A.L.J. Pereira, L. Gracia, A. Beltrán, P.N. Lisboa-Filho, J.H.D. da Silva, J. Andrés, *J. Phys. Chem. C* **116**, 8753–8762 (2012)
22. P. Merle, J. Pascual, J. Camassel, H. Mathieu, *Phys. Rev. B* **21**, 1617 (1980)
23. X.Y. Li, H.J. Li, Z.J. Wang, H. Xia, Z.Y. Xiong, J.X. Wang, B.C. Yang, *Opt. Commun.* **282**, 247 (2009)
24. P. Salvador, *Sol. Energy Mater.* **6**, 241 (1982)
25. C.M. Maghanga, G.A. Niklasson, C.G. Granqvist, *Thin Solid Films* **518**, 1254–1258 (2009)
26. Y. Sato, H. AKizuki, T. Kamiyama, Y. Shigesato, *Thin Solid Films* **516**, 5758–5762 (2008)
27. K.-H. Hung, P.-W. Lee, W.-C. Hsu, H.C. Hsing, H.-T. Chang, M.-S. Wong, *J. Alloys Compd.* **509**, 10190–10194 (2011)
28. T.S. Moss, *Proc. Phys. Soc. B* **67**, 775–782 (1954)
29. Y. Zhang, Y. Shen, F. Gu, M. Wu, Y. Xie, J. Zhang, *Appl. Surf. Sci.* **256**, 85–89 (2009)
30. K. Boubaker, *Eur. Phys. J. Plus* **126**, 1–4 (2011)
31. S. Sebastian, M.A. Khadar, *Bull. Mater. Sci.* **27**, 207–212 (2004)
32. G. Haacke, *J. Appl. Phys.* **47**, 4086 (1976)